



CHORUS

This is the accepted manuscript made available via CHORUS. The article has been published as:

Thermographic measurements of spin-current-induced temperature modulation in metallic bilayers

R. Iguchi, A. Yagmur, Y.-C. Lau, S. Daimon, E. Saitoh, M. Hayashi, and K. Uchida

Phys. Rev. B **98**, 014402 — Published 2 July 2018

DOI: [10.1103/PhysRevB.98.014402](https://doi.org/10.1103/PhysRevB.98.014402)

1 Thermographic measurements of spin-current-induced temperature 2 modulation in metallic bilayers

3
4 R. Iguchi^{1,*}, A. Yagmur^{1,2,*}, Y.-C. Lau^{1,3}, S. Daimon^{2,4,5}, E. Saitoh^{2,4,7}, M. Hayashi^{1,3}, and K. Uchida^{1,6,8,†}

5 ¹*National Institute for Materials Science, Tsukuba 305-0047, Japan*

6 ²*Institute for Materials Research, Tohoku University, Sendai 980-8577, Japan*

7 ³*Department of Physics, The University of Tokyo, Tokyo 113-0033, Japan*

8 ⁴*Department of Applied Physics, The University of Tokyo, Tokyo 113-8656, Japan*

9 ⁵*Advanced Institute for Materials Research, Tohoku University, Sendai 980-8577, Japan*

10 ⁶*Center for Spintronics Research Network, Tohoku University, Sendai 980-8577, Japan*

11 ⁷*Advanced Science Research Center, Japan Atomic Energy Agency, Tokai 319-1195, Japan*

12 ⁸*Department of Mechanical Engineering, The University of Tokyo, Tokyo 113-8656, Japan*

13
14 Temperature modulation due to a pure spin current has been investigated in bilayer metallic films consisting of a
15 paramagnetic metal (PM; Pt, W, or Ta) and a ferromagnetic metal (FM; CoFeB or permalloy). When a charge
16 current is applied to the PM/FM bilayer film, a spin current is generated across the PM/FM interface owing to the
17 spin Hall effect in PM. The spin current was found to exhibit cooling and heating features depending on the sign
18 of the spin Hall angle of PM; the spin-current-induced temperature modulation is estimated by subtracting the
19 contribution of the anomalous Ettingshausen effect in FM monolayer films, and attributed to the conduction-
20 electron-driven spin-dependent Peltier effect and magnon-driven spin Peltier effect in FM. To reveal the origin of
21 the spin-current-induced contribution in the PM/FM films, we compared the experimental results with the
22 phenomenological calculations based on the spin and magnon diffusion models. We found that the spin-current-
23 induced temperature modulation is greater than that expected from the spin-dependent Peltier coefficients reported
24 in earlier studies and its characteristic length is around 10 nm, possibly larger than typical spin diffusion lengths
25 of conduction electrons in FM. These facts indicate that the signals in the PM/FM films contain the substantial
26 contribution from the magnon-driven spin Peltier effect.

27
28 * These authors contributed equally to this work.

29 † UCHIDA.Kenichi@nims.go.jp

1 I. INTRODUCTION

2 The field of spin caloritronics aims to develop novel physics and applications based on the interplay
3 between spintronics and thermal transport effects [1–11]. Experimental studies on spin caloritronics begin with
4 the investigation of heat-to-spin current conversion phenomena. One of such phenomena is the spin Seebeck
5 effect (SSE), which refers to the generation of a spin current as a result of a heat current in magnetic
6 materials [12–25]. Since the SSE appears in magnetic insulators, this phenomenon is now understood in terms of
7 non-equilibrium thermal magnon transport, and most of the experimental behaviors are explained by the magnon-
8 based models [26–35]. In addition to the magnon-driven SSE, the heat-to-spin current conversion can arise also
9 from conduction-electrons’ spin transport; this is called the spin-dependent Seebeck effect (SdSE) because it
10 originates from the difference in Seebeck coefficients between up- and down-spin electrons [3]. After the
11 pioneering demonstration of the spin dependence of the Seebeck coefficient by Slachter *et al.*, the SdSE has been
12 investigated in several ferromagnetic metals [36–39].

13 Another important topic in spin caloritronics is the investigation of the inverse effects: the spin-to-heat
14 current conversion phenomena. This stream is accelerated by the direct observation of the spin-dependent Peltier
15 effect (SdPE), the Onsager reciprocal of the SdSE, in ferromagnetic metal (FM)/paramagnetic metal (PM)/FM
16 pillar structures by Flipse *et al.* [40]. In 2014, they also reported the observation of the spin Peltier effect (SPE) in
17 Pt/ferrimagnetic insulator [yttrium iron garnet (YIG)] junctions by using micro-fabricated thermopile sensors [41].
18 The SdPE and SPE refer to the generation of a heat current as a result of a spin current and, in analogy with the
19 heat-to-spin current conversion phenomena, the mechanism of the SdPE (SPE) is discussed in terms of non-
20 equilibrium transport of conduction-electrons’ spins (magnons). Namely, the SdPE originates from the spin-
21 dependent difference in the Peltier coefficient in FM, while the SPE from the energy flow concomitant with
22 magnon dynamics [Figs. 1(a) and 1(b)]. However, the experimental research on the spin-to-heat current
23 conversion phenomena is limited to a few studies [3,42–46], and their behaviors and mechanisms are not
24 sufficiently investigated. This situation is attributed mainly to difficulty in measuring the SdPE and SPE; the spin-
25 current-induced temperature change appears in nanoscale thin film devices and its magnitude is typically smaller
26 than 10 mK [40]. The conventional temperature measurements in such nanoscale devices also have difficulty in
27 quantitative estimation of the spin-to-heat current conversion efficiency because the temperature modulation
28 concomitant with spin currents is confined near heat-source positions [43].

1 To overcome this situation, we have recently established a versatile method for measuring the SPE based
2 on the lock-in thermography (LIT) technique [43–45]. This method allows imaging of the temperature modulation
3 induced by the SPE with high temperature and spatial resolutions (< 0.1 mK and < 20 μm in this study) and
4 requires no micro-fabrication processes, realizing systematic investigations of the spin-to-heat current conversion
5 properties. In Refs. [43,45], by using the LIT method, we have systematically investigated the temperature
6 modulation induced by the SPE in PM/YIG junctions and revealed its unconventional spatial distribution.
7 However, the investigation of the spin-to-heat current conversion phenomena using the LIT method has been
8 performed only for magnetic insulators, where the spin-to-heat current conversion arises only from the magnon-
9 driven SPE because of the absence of the conduction-electrons' contribution.

10 In this work, we have applied the LIT method to PM/FM bilayer films and investigated the spin-to-heat
11 current conversion phenomena in metallic systems. The spin-to-heat current conversion in metallic systems is
12 more complicated than that in insulating systems since it can be driven by both the conduction-electron-driven
13 SdPE and magnon-driven SPE and be contaminated by thermoelectric effects in FM. The systematic
14 measurements based on the LIT provide a crucial piece of information for separating these contributions and
15 clarifying the spin-to-heat current conversion mechanisms in metals.

16 This paper is organized as follows. In Sec. II, we explain the details of the experimental procedures and
17 configurations for the measurements of the spin-to-heat current conversion phenomena using the LIT method. In
18 Sec. III, we report the observation of the spin-current-induced temperature modulation in PM/FM bilayer films,
19 followed by model calculations to discuss the origin of the observed behaviors. The last Sec. IV is devoted to the
20 conclusion of the present study.

22 II. EXPERIMENTAL PROCEDURE AND CONFIGURATION

23 The sample system used in this study consists of a PM film formed on a FM film. Here, we select two
24 different FM materials. The first one is $\text{Co}_{20}\text{Fe}_{60}\text{B}_{20}$ (CoFeB), which is known to have large difference in spin-
25 dependent Seebeck/Peltier coefficients [47,48]. The other one is $\text{Ni}_{81}\text{Fe}_{19}$ [permalloy (Py)], which is a typical FM
26 with moderate difference in spin-dependent Seebeck/Peltier coefficients [49]. As the PM layer, we select Pt, W,
27 and Ta since they have strong spin-orbit coupling, of which the sign for Pt is opposite to that for W and Ta. The
28 thickness of the PM (FM) layer is 10 nm (20 nm) except for the samples used for the measurements of the
29 thickness dependence shown in Sec. IIIB. The PM/FM bilayer films were fabricated on sapphire substrates and

1 patterned into U-shaped structure by sputtering the PM and FM layers through a metallic shadow mask [Figs. 2(a)
 2 and 2(b)], where the line-width of the U-shaped structure is 0.2 mm and the total line length of U-shaped structure
 3 is $l_{\text{tot}} = 4.6$ mm. To avoid the oxidation, Ta(1 nm)/MgO(2 nm) protective layers were sputtered on the PM layer,
 4 where the MgO layer is used since MgO is known to form a sharp interface with CoFeB and the Ta layer is used
 5 to protect the MgO layer. Since the Ta layer is oxidized under ambient condition and becomes resistive, it does
 6 not affect the transport properties in the PM/FM system.

7 In the PM/FM bilayer film, both the conduction-electron-driven SdPE and magnon-driven SPE can
 8 contribute to the spin-to-heat current conversion. To excite the SdPE and SPE in the PM/FM system, we employ
 9 the spin Hall effect (SHE) [50–54] in the PM layer for injecting a spin current into the FM layer [Figs. 1(a) and
 10 1(b)]. In the previous studies using magnetic pillar structures [40], the SdPE has been excited by a spin-polarized
 11 current accompanied by a finite charge current. In contrast, the spin-to-heat current conversion in our PM/FM
 12 system is excited by a pure spin current induced by the SHE. In this study, despite the difference in the input
 13 currents, we refer to the spin-to-heat current conversion driven by conduction electrons as the SdPE because of the
 14 same origin. When a charge current \mathbf{J}_c with its density vector \mathbf{j}_c flows in the PM layer of the PM/FM system along
 15 the y direction, a spin current \mathbf{J}_s with its density vector \mathbf{j}_s and the spin-polarization vector $\boldsymbol{\sigma}$ is generated due to the
 16 SHE in PM and injected into FM. Here, electrons with $\boldsymbol{\sigma}$ along the x direction induce \mathbf{J}_s along the z direction,
 17 since the SHE holds the following relation

$$\mathbf{j}_s = \theta_{\text{SH}} \mathbf{j}_c \times \boldsymbol{\sigma}, \quad (1)$$

18 where θ_{SH} is the spin Hall angle of PM. In the SdPE (SPE), the spin current in FM is carried by conduction
 19 electrons (magnons). When the $\boldsymbol{\sigma}$ direction is parallel or antiparallel to the magnetization \mathbf{M} of FM, the spin
 20 current induces a temperature gradient along the stacking direction, i.e., the z direction. Here, the magnitude of the
 21 temperature gradient is proportional to $|\mathbf{J}_s|$ and its direction is dependent on the $\boldsymbol{\sigma}$ direction and the sign of the
 22 SdPE or SPE coefficient. As shown in Figs. 1(a) and 1(b), the symmetry of the SHE-driven SdPE is the same as
 23 that of the SPE; both effects can be superimposed. To realize the detection of the SdPE and SPE in the PM/FM
 24 system, it is also important to distinguish their signals from the anomalous Ettingshausen effect (AEE), which is a
 25 transverse thermoelectric effect occurring in FM [55]. Since the temperature gradient due to the AEE in FM is
 26 generated in the direction of the cross product of \mathbf{J}_c and \mathbf{M} , it contaminates the SdPE and SPE signals in the
 27 PM/FM bilayer systems [Fig. 1(c)]. We separate the spin-current-induced signals from the AEE signals by
 28 comparing the results in the PM/FM systems with those in FM monolayer films, where only the AEE contribution
 29 exists (see Sec. IIIA for details).

1 To detect the temperature change induced by the spin current in the PM/FM samples, we performed the
2 LIT measurements at room temperature and atmospheric pressure [56,57]. First of all, the surface of the samples
3 was coated with insulating black ink to enhance infrared emissivity. In the LIT measurements, we measured the
4 spatial distribution of infrared radiation thermally emitted from the surface of the U-shaped PM/FM films with
5 applying a rectangularly-modulated AC voltage with the amplitude V , frequency f , and zero DC offset to the films
6 [Fig. 2(a)]. In this study, we fixed the lock-in frequency at $f = 5$ Hz. By extracting the first harmonic response of
7 detected thermal images via Fourier analyses, we can obtain the lock-in amplitude A and phase ϕ images,
8 enabling highly-sensitive detection of thermo-spin and thermoelectric effects free from the Joule-heating
9 background [Fig. 2(a)] [43,45]. Here, the A (ϕ) image provides the spatial distribution of the magnitude of the
10 voltage-induced temperature modulation (the sign of the temperature modulation as well as the time delay due to
11 thermal diffusion), where the A (ϕ) values are defined in the ranges of $A \geq 0$ ($0^\circ \leq \phi < 360^\circ$). During the LIT
12 measurements, to saturate the magnetization \mathbf{M} of the CoFeB and Py films along the magnetic field \mathbf{H} , we applied
13 an in-plane magnetic field H with the magnitude of $|H| > 0.5$ kOe along the x direction [see the magnetization
14 curve of the CoFeB film shown in Fig. 2(c)]. To extract the pure SdPE, SPE, and AEE contributions, which
15 reverse sign by reversing \mathbf{H} , we calculated the A_{odd} and ϕ_{odd} images showing the distribution of the voltage-
16 induced temperature modulation with the H -odd dependence. Here, the A_{odd} and ϕ_{odd} images are obtained by
17 subtracting the LIT images at $H < -0.5$ kOe from those at $H > +0.5$ kOe and dividing the subtracted images by 2.
18 In our samples, owing to the U-shaped structure, the symmetries of the SdPE, SPE, and AEE can be confirmed
19 simultaneously because the relative orientation of \mathbf{J}_c and \mathbf{M} is different between the areas L, R, and C, where $\mathbf{J}_c \perp$
20 \mathbf{M} on L and R and $\mathbf{J}_c \parallel \mathbf{M}$ on C when \mathbf{M} is along the x direction [Fig. 2(b)]. Therefore, the temperature modulation
21 due to the SdPE, SPE, and AEE appears on L and R, while it disappears on C [43,45]. Since the \mathbf{J}_c direction on L
22 is opposite to that on R, the sign of the temperature modulation induced by these phenomena is reversed between
23 these areas.

24

25 III. RESULTS AND DISCUSSION

26 A. Separation of spin-current-induced temperature modulation from AEE in PM/CoFeB systems

27 Figures 2(d) and 2(e) respectively show the A_{odd} and ϕ_{odd} images for the Pt/CoFeB film at $V = 10$ V and $|H| =$
28 1.4 kOe, where $V = 10$ V corresponds to the electric field magnitude E of 2.2 kV/m and the charge-current

1 amplitude of 20 mA for this sample. We observed clear temperature-modulation signals on L and R, where
2 $\mathbf{J}_c \perp \mathbf{M}$, and $\sim 180^\circ$ difference in ϕ between L and R, while the signals disappear on C, where $\mathbf{J}_c \parallel \mathbf{M}$. Since the
3 heat-conduction condition is the same for L and R, this ϕ shift is irrelevant to the time delay caused by thermal
4 diffusion, indicating that the sign of the temperature modulation is reversed depending on the direction of \mathbf{J}_c . In
5 Figs. 2(f) and 2(g), we show the V dependence of A_{odd} and ϕ_{odd} in the Pt/CoFeB film, respectively. The A_{odd} value
6 is proportional to V , while the ϕ_{odd} shift of $\sim 180^\circ$ remains unchanged with respect to V . These behaviors are in
7 good agreement with the features of the SPE, SdPE, and AEE [40,41,43–45,55].

8 To clarify the origin of the temperature modulation in the Pt/CoFeB film, we performed the control
9 experiments using a CoFeB monolayer film, without the PM layer, and a W/CoFeB (Ta/CoFeB) bilayer film in
10 which the Pt layer is replaced with the W (Ta) layer. As shown in Figs. 3(a) and 3(b), we found that the CoFeB,
11 W/CoFeB, and Ta/CoFeB films exhibit the clear temperature modulation with the same symmetry and sign as
12 those for the Pt/CoFeB film. In contrast, the signal magnitude depends on the sample species; the A_{odd} values on L
13 and R for the Pt/CoFeB film (W/CoFeB and Ta/CoFeB films) are greater (smaller) than those for the CoFeB
14 monolayer, which contain only the AEE contribution [Figs. 3(a) and 3(c)]. This result indicates that the positive
15 (negative) spin-current-induced contribution driven by the SHE in Pt (W and Ta) is superimposed on the positive
16 AEE background in the CoFeB layer, since the sign of θ_{SH} in Pt (W and Ta) is positive (negative) and the PM
17 layer exhibits no AEE (note that the H -linear contribution of the ordinary Ettingshausen effect in PM is negligibly
18 small [45,55]). Importantly, during the LIT measurements, we fixed the amplitude of the voltage V , not the charge
19 current, applied to the PM/CoFeB and CoFeB films; if we regard the PM/CoFeB bilayer film as a simple parallel
20 circuit comprising the PM and CoFeB layers with negligible interface resistivity [58], the charge-current density
21 and resultant AEE contribution in the CoFeB layer of the PM/CoFeB bilayers is the same as that in the CoFeB
22 monolayer. Based on this interpretation, we estimate the spin-current-induced contribution in the PM/CoFeB films
23 by subtracting the signal in the CoFeB monolayer from that in the PM/CoFeB bilayers. As shown in Fig. 3(d), the
24 subtracted LIT amplitude per unit electric field $\Delta A_{\text{odd}}/E$ with $E = V/l_{\text{tot}}$ in the Pt/CoFeB film (W/CoFeB and
25 Ta/CoFeB films) exhibit the clear positive (negative) contribution, consistent with the characteristic of the SPE
26 and SdPE. Here, the sign of the spin-current-induced signal in the Pt/CoFeB film is the same as that of the SPE
27 signal in the Pt/YIG system [43].

1 **B. Thickness dependence of spin-current-induced temperature modulation and AEE**

2 In this subsection, we show the thickness dependence of the voltage-induced temperature modulation. First, to
3 further support our interpretation that the ΔA_{odd} signals in the PM/CoFeB films originate from the SHE in the PM
4 layer, we investigated the PM-layer thickness dependence of the temperature modulation. Here, we used the
5 W/CoFeB films with the different W-layer thickness d_{W} and the constant CoFeB-layer thickness of 20 nm.
6 Figures 4(a) and 4(b) show the A_{odd} and \square_{odd} images for the CoFeB monolayer and W(d_{W})/CoFeB films at $V = 10$
7 V and $|H| = 0.7$ kOe. We observed clear temperature-modulation signals with the aforementioned features in all
8 the films. As shown in Fig. 4(c), the magnitude of the A_{odd} signals in the W(d_{W})/CoFeB films is smaller than that
9 in the CoFeB monolayer film. To quantitatively estimate the d_{W} dependence of the signal reduction, ΔA_{odd} , we
10 normalized the ΔA_{odd} signals by the charge-current density j_{c}^{W} in the W layer, based on the parallel circuit
11 model [58]. As shown in Fig. 4(d), the magnitude of $\Delta A_{\text{odd}}/j_{\text{c}}^{\text{W}}$ for the W(5 nm)/CoFeB film is much greater than
12 that for the W(10 or 15 nm)/CoFeB films and the resistivity of the 5-nm-thick W film is much greater than that of
13 the 10- and 15-nm-thick films. This behavior is consistent with the W-thickness dependence of θ_{SH} ; the SHE in W
14 is known to be enhanced with decreasing the thickness due to the contribution from the highly-resistive β -W
15 phase [59–61]. The W-thickness dependence observed here buttresses our basis that the difference in the
16 temperature modulation between the PM/CoFeB bilayer and CoFeB monolayer films is attributed to the spin-
17 current injection induced by the SHE.

18 Next, we measured the FM-layer thickness dependence of the spin-current-induced temperature modulation to
19 investigate the length scale of the observed phenomena. To do this, we performed the same experiments using the
20 Pt/CoFeB and CoFeB films with varying the CoFeB thickness d_{CoFeB} while fixing the Pt thickness at 10 nm.
21 Figure 5(a) shows the d_{CoFeB} dependence of A_{odd}/E for the Pt/CoFeB(d_{CoFeB}) and CoFeB(d_{CoFeB}) films at $|H| = 1.4$
22 kOe. We observed clear temperature-modulation signals in all the films and found that the magnitude of A_{odd}/E
23 monotonically increases with increasing d_{CoFeB} . The AEE signal in the CoFeB monolayer films exhibits an almost
24 linear dependence on d_{CoFeB} ; this behavior can be explained simply by the facts that the out-of-plane heat current
25 induced by the AEE is constant in the CoFeB layer and that the resultant temperature difference is proportional to
26 the integral of the heat current over the CoFeB thickness. In contrast, the d_{CoFeB} dependence of the spin-current-
27 induced signal in the Pt/CoFeB films, extracted by subtracting the AEE contributions in the CoFeB layer, shows a
28 different behavior; as shown in Fig. 5(b), the magnitude of $\Delta A_{\text{odd}}/j_{\text{c}}^{\text{Pt}}$ in the Pt/CoFeB films gradually increases
29 with increasing d_{CoFeB} but saturates when $d_{\text{CoFeB}} > 30$ nm, where j_{c}^{Pt} denotes the charge-current density in the Pt
30 layer. This saturation behavior is qualitatively similar to the ferromagnetic- or ferrimagnetic-layer thickness

1 dependence of the thermo-spin effects, such as the SSE, SdSE, and SPE [30,45,62] (note that non-monotonical
2 thickness dependence may appear when the decay length of spin and energy is separated, e.g. in Pt/YIG
3 systems [63]). In Sec. IIID, we discuss the origin of the d_{CoFeB} dependence of the spin-current-induced signals by
4 using model calculations.

5 C. Comparison between Pt/CoFeB and Pt/Py systems

6 The above experiments clearly show that the PM/CoFeB films exhibit the spin-current-induced temperature
7 modulation. However, the temperature modulation may include both the conduction-electron-driven SdPE and
8 magnon-driven SPE contributions in the metallic samples. To obtain a clue for distinguishing the SdPE and SPE
9 contributions, we measured the spin-current-induced temperature modulation also in the Pt/Py film under the
10 same conditions as the CoFeB experiments. Since the SdPE coefficient of Py is believed to be much smaller than
11 that of CoFeB [48,49,64], the SdPE contribution in the Pt/Py films is expected to be smaller than that in the
12 Pt/CoFeB films.

13 In Figs. 6(a) and 6(b), we show the A_{odd} and \square_{odd} images for the Py monolayer and Pt/Py bilayer films at $V =$
14 10 V and $|H| = 1.4$ kOe. Both the samples exhibit clear temperature-modulation signals on L and R in the same
15 manner as the CoFeB experiments, where the sign of the signals is reversed between L and R [Fig. 6(b)] and the
16 magnitude is proportional to V [Fig. 6(c)]. Importantly, the signal magnitude in the Pt/Py bilayer film was found
17 to be greater than that in the Py monolayer film, indicating the finite spin-current contribution in the Pt/Py film.
18 As shown in the inset to Fig. 6(c), the ΔA_{odd} signal in the Pt/Py film is proportional to V , consistent with the
19 characteristic of the SPE and SdPE. The sign of the spin-current-induced temperature modulation in the Pt/Py film
20 is the same as that in the Pt/CoFeB film.

21 Here, we compare the magnitude of the spin-current-induced temperature modulation between the Pt/CoFeB
22 and Pt/Py films. The values of $\Delta A_{\text{odd}}/j_c^{\text{Pt}}$ on L for the Pt(10nm)/CoFeB(20nm) and Pt(10nm)/Py(20nm) films are
23 estimated to be $0.71 \times 10^{-13} \text{ Km}^2\text{A}^{-1}$ and $0.32 \times 10^{-13} \text{ Km}^2\text{A}^{-1}$, respectively. The magnitude of the spin-current-
24 induced signal in the Pt/CoFeB film is greater than but comparable to that in the Pt/Py film despite the substantial
25 difference in electron-transport properties between CoFeB and Py [48,49]. Furthermore, as discussed in Sec. IIID,
26 the magnitude of the spin-current-induced temperature modulation observed here is too large to be explained only
27 by the SdPE contribution. These facts imply that not only the conduction-electron-driven SdPE but also the
28 magnon-driven SPE contributes to the temperature modulation in our PM/FM bilayer films.

1 **D. Modeling of SdPE- and SPE-induced temperature modulation**

2 To further discuss the origin of the observed spin-current-induced temperature modulation, we model the
 3 SHE-induced SdPE and SPE in the PM/FM bilayer films. The spin currents in FM are composed of conduction
 4 electrons and magnons. For conduction electrons in FM, the diffusive spin current is driven by the gradient of the
 5 spin-dependent electrochemical potentials μ_σ with the spin index σ ($= \uparrow, \downarrow$) as follows:

$$j_s = -\left(\sigma_\uparrow \nabla \frac{\mu_\uparrow}{e} - \sigma_\downarrow \nabla \frac{\mu_\downarrow}{e}\right) = -\frac{\sigma_{\text{FM}}}{2} \nabla \frac{\mu_s}{e} - \sigma_{\text{FM}} P_{\text{FM}} \nabla \frac{\mu_c}{e}, \quad (2)$$

6 where $\mu_s = \mu_\uparrow - \mu_\downarrow$, $\mu_c = (\mu_\uparrow + \mu_\downarrow)/2$, e is the elemental charge, $\sigma_{\text{FM}} = \sigma_\uparrow + \sigma_\downarrow$ the electrical conductivity, and P_{FM}
 7 the spin polarization of conduction electrons: $P_{\text{FM}} = (\sigma_\uparrow - \sigma_\downarrow)/\sigma_{\text{FM}}$. When no charge current exists along the spin
 8 current, this spin current gives rise to the SdPE-induced temperature modulation: $\Delta T_{\text{SdPE}} \propto -\Pi_s j_s$ with the SdPE
 9 coefficient Π_s , which is determined by the difference in the Peltier coefficient between the up- and down-spin
 10 conduction electrons: $\Pi_s = \Pi_\uparrow - \Pi_\downarrow$. Magnons can also be driven by the gradient of its accumulation μ_m , and the
 11 magnon current is given by

$$j_m = -\sigma_m \nabla \frac{\mu_m}{e}, \quad (3)$$

12 where σ_m is the magnon conductivity. The SPE-induced temperature change is described as $\Delta T_{\text{SPE}} \propto \Pi_{\text{SPE}} j_m$ with
 13 the SPE coefficient Π_{SPE} .

14 To estimate the SdPE- and SPE-induced temperature modulations, we determined the spin-current density
 15 by solving the diffusion equations for μ_s , μ_c , and μ_m :

$$\begin{aligned} \nabla^2 \mu_s &= \mu_s / \lambda^2 \\ \nabla^2 \mu_c &= 0 \\ \nabla^2 \mu_m &= \mu_m / \lambda_m^2, \end{aligned} \quad (4)$$

16 where λ (λ_m) is the spin (magnon) diffusion length. We consider one-dimensional spin and magnon transports in
 17 the direction perpendicular to the PM/FM interface (the z direction). The FM (PM) layer possesses the
 18 conductivity $\sigma_{\text{FM(PM)}}$, spin diffusion length $\lambda_{\text{FM(PM)}}$, and thickness $d_{\text{FM(PM)}}$, where the FM (PM) layer is in the range
 19 of $-d_{\text{FM}} \leq z \leq 0$ ($0 \leq z \leq d_{\text{PM}}$). The boundary conditions are given by $j_s^{\text{FM}}(-d_{\text{FM}}) = 0$, $j_m(-d_{\text{FM}}) = 0$, $j_s^{\text{PM}}(d_{\text{PM}}) + j_s^{\text{SHE}}$
 20 $= 0$, $\nabla \mu_c = 0$ at the system edges, and $j_s^{\text{FM}}(0) + j_m(0) = j_s^{\text{PM}}(0) + j_s^{\text{SHE}}$, where j_s^{SHE} and $j_s^{\text{FM(PM)}}(z)$ denote the spin
 21 current induced by the SHE and the spin current in FM (PM) along the z direction, respectively. We describe the
 22 spin-magnon interconversions at the PM/FM interface ($z = 0$) as

$$j_s^{\text{FM}}(0) = G_s [\mu_s^{\text{FM}}(0) - \mu_s^{\text{PM}}(0)] / e, \quad (5)$$

$$j_m(0) = G_m[\mu_m(0) - \mu_s^{\text{PM}}(0)]/e, \quad (6)$$

1 where $\mu_s^{\text{FM(PM)}}(z)$ denotes the spin accumulation in FM (PM) [30,33,65]. G_s (G_m) represents the conductance for
 2 the interconversion between conduction electrons spins in PM and FM (between conduction electron spins in PM
 3 and magnons in FM). Subsequently, we obtain

$$j_s^{\text{FM}} = -\frac{G_s \Gamma_{\text{FM}}}{(G_s + \Gamma_{\text{FM}})} \frac{\sinh\left(\frac{[d_{\text{FM}}+z]}{\lambda_{\text{FM}}}\right)}{\sinh\left(\frac{d_{\text{FM}}}{\lambda_{\text{FM}}}\right)} \frac{\mu_s^{\text{PM}}(0)}{e}, \quad (7)$$

$$j_s^{\text{PM}} = -\frac{\cosh\left(\frac{z}{\lambda_{\text{PM}}}\right)}{\cosh\left(\frac{d_{\text{PM}}}{\lambda_{\text{PM}}}\right)} j_s^{\text{SHE}} + \Gamma_{\text{PM}} \frac{\sinh\left(\frac{[d_{\text{PM}}-z]}{\lambda_{\text{PM}}}\right)}{\sinh\left(\frac{d_{\text{PM}}}{\lambda_{\text{PM}}}\right)} \frac{\mu_s^{\text{PM}}(0)}{e}, \quad (8)$$

$$j_m = -\frac{G_m \Gamma_m}{(G_m + \Gamma_m)} \frac{\sinh\left(\frac{[d_{\text{FM}}+z]}{\lambda_m}\right)}{\sinh\left(\frac{d_{\text{FM}}}{\lambda_m}\right)} \frac{\mu_s^{\text{PM}}(0)}{e}, \quad (9)$$

4 where $\Gamma_{\text{FM}} = (1 - P_{\text{FM}}^2) \frac{\sigma_{\text{FM}} \tanh\left(\frac{d_{\text{FM}}}{\lambda_{\text{FM}}}\right)}{2\lambda_{\text{FM}}}$, $\Gamma_{\text{PM}} = \frac{\sigma_{\text{PM}} \tanh\left(\frac{d_{\text{PM}}}{\lambda_{\text{PM}}}\right)}{2\lambda_{\text{PM}}}$, $\Gamma_m = \frac{\sigma_m \tanh\left(\frac{d_{\text{FM}}}{\lambda_m}\right)}{\lambda_m}$, and

$$\mu_s^{\text{PM}}(0) = -\frac{e j_s^{\text{SHE}} \left(1 - \text{sech}\left(\frac{d_{\text{PM}}}{\lambda_{\text{PM}}}\right)\right)}{\left[\Gamma_{\text{PM}} + \frac{G_s \Gamma_{\text{FM}}}{(G_s + \Gamma_{\text{FM}})} + \frac{G_m \Gamma_m}{(G_m + \Gamma_m)}\right]}. \quad (10)$$

5 The resulting temperature modulation $\delta T_{\text{SdPE(SPE)}}$ due to the SdPE (SPE) at the surface of the system can be
 6 obtained as

$$\begin{pmatrix} \delta T_{\text{SdPE}} \\ \delta T_{\text{SPE}} \end{pmatrix} = \frac{1}{\kappa_{\text{FM}}} \int_{z=-d_{\text{FM}}}^{z=0} \begin{pmatrix} -\frac{\Pi_s}{2} j_s \\ \Pi_{\text{SPE}} j_m \end{pmatrix} dz \quad (11)$$

7 by solving the one-dimensional heat equation with assuming that the bottom of the PM/FM film is connected to a
 8 heat bath (i.e., the substrate) and top surface of the film is open, where κ_{FM} is the thermal conductivity of FM.

9 Note that the temperature modulation in the black ink layer can be omitted because there is negligibly small heat
 10 current as the heat radiation loss from the top surface is not effective compared with bulk thermal conduction.

11 Finally, the temperature modulation induced by the SdPE is given by

$$\delta T_{\text{SdPE}} = -\frac{\Pi_s}{2\kappa_{\text{FM}}} \frac{G_s \Gamma_{\text{FM}}}{(G_s + \Gamma_{\text{FM}})} \frac{j_s^{\text{SHE}} \lambda_{\text{FM}} \tanh\left(\frac{d_{\text{FM}}}{2\lambda_{\text{FM}}}\right) \left(1 - \text{sech}\left(\frac{d_{\text{PM}}}{\lambda_{\text{PM}}}\right)\right)}{\left[\Gamma_{\text{PM}} + \frac{G_s \Gamma_{\text{FM}}}{(G_s + \Gamma_{\text{FM}})} + \frac{G_m \Gamma_m}{(G_m + \Gamma_m)}\right]} \quad (12)$$

12 and that induced by the SPE is given by

$$\delta T_{\text{SPE}} = \frac{\Pi_{\text{SPE}}}{\kappa_{\text{FM}}} \frac{G_m \Gamma_m}{(G_m + \Gamma_m)} \frac{j_s^{\text{SHE}} \lambda_m \tanh\left(\frac{d_{\text{FM}}}{2\lambda_{\text{FM}}}\right) \left(1 - \text{sech}\left(\frac{d_{\text{PM}}}{\lambda_{\text{PM}}}\right)\right)}{\left[\Gamma_{\text{PM}} + \frac{G_s \Gamma_{\text{FM}}}{(G_s + \Gamma_{\text{FM}})} + \frac{G_m \Gamma_m}{(G_m + \Gamma_m)}\right]}. \quad (13)$$

1 Here, it is noteworthy that Γ_{FM} and Γ_{m} depends on d_{FM} . The contribution from the interfacial thermal resistance
 2 can be included by

$$\delta T_{\text{SdPE}}^{\text{int}} = -\frac{\Pi_{\text{s}} j_{\text{s}}^{\text{FM}} \big|_{z=0}}{2\kappa_{\text{int}}}, \quad (14)$$

3 assuming continuity of the heat current at the PM/FM interface and the FM layer. The same manner can be
 4 applied to the SPE.

5 The above model calculations show that the SdPE and SPE have quite similar d_{FM} dependence. Although the
 6 difference between the SdPE and SPE comes from the transport properties of conduction electron spins and
 7 magnons, such as the length scale, conductivity, and conversion efficiencies at the interface, and the SdPE and
 8 SPE coefficients, it is difficult to estimate the SdPE and SPE parameters simultaneously by fitting; a number of
 9 parameters have to be assumed for quantitative discussions (see below). The experimental results in Fig. 5(b)
 10 show that the d_{FM} dependence of $\Delta A_{\text{odd}}/j_{\text{c}}^{\text{Pt}}$ in the Pt/CoFeB films has a characteristic length of ~ 10 nm, which is
 11 similar to or rather longer than λ_{FM} for CoFeB, obtained in spin-valve experiments at low temperatures [66–68].
 12 As the diffusion length of magnons can be larger than that of electron spins owing to the difference in the
 13 scattering mechanisms [30,33,62,66,69,70], the observed $\Delta A_{\text{odd}}/j_{\text{c}}^{\text{Pt}}$ signals may contain the contribution from the
 14 magnon-driven SPE. Nevertheless, it is still difficult to separate the SdPE and SPE contributions quantitatively
 15 because of the presence of unknown transport parameters.

16 To obtain a clue for the separation, we estimated the spin-to-heat conversion coefficient from the magnitude
 17 of the observed $\Delta A_{\text{odd}}/j_{\text{c}}^{\text{Pt}}$ signal. First of all, we have to note that, to compare with the model calculation with the
 18 LIT results, the amplitude j_{c}^{Pt} of the square wave should be converted into the amplitude of the first harmonic
 19 sinusoidal wave: $(4/\pi)j_{\text{c}}^{\text{Pt}}$. If we attributed the signal for the Pt/CoFeB film solely to the SdPE, we obtained
 20 $\Pi_{\text{s}}/\kappa_{\text{CoFeB}} = (-5.1 \pm 0.8) \times 10^{-3} \text{ VKmW}^{-1}$ and $\lambda_{\text{CoFeB}} = 9.4 \pm 4.6 \text{ nm}$ from the fitting using the experimental values of
 21 $\sigma_{\text{CoFeB}} = 6.0 \times 10^5 \text{ } \Omega^{-1}\text{m}^{-1}$ [see the inset to Fig.5(b)], $\sigma_{\text{Pt}} = 3.8 \times 10^6 \text{ } \Omega^{-1}\text{m}^{-1}$, which is estimated based on the short-
 22 circuit model, and $d_{\text{Pt}} = 10 \text{ nm}$ and the reference values of $P_{\text{FM}} = 0.72$ [64], $\lambda_{\text{Pt}} = 2 \text{ nm}$ [53], and $\theta_{\text{SH}}=0.2$ [71],
 23 where the fitting result is shown with a red solid line in Fig. 5(b). Here, κ_{CoFeB} and λ_{CoFeB} are the thermal
 24 conductivity and spin diffusion length of CoFeB, respectively. We assume an infinitely large G_{s} , the condition in
 25 which μ_{s} is continuous at the PM/FM interface, and the lower limit of Π_{s} is obtained. If κ_{CoFeB} is comparable to the
 26 thermal conductivity of CoFe, i.e., assuming $\kappa_{\text{CoFeB}} = 29.8 \text{ Wm}^{-1}\text{K}^{-1}$ [49], we obtained $\Pi_{\text{s}} = -0.152 \pm 0.023 \text{ V}$. The
 27 $\Pi_{\text{s}}/\kappa_{\text{Py}}$ value for Py is estimated to be $(-5.2 \pm 2.0) \times 10^{-4} \text{ VKmW}^{-1}$ from the experimental values of $\sigma_{\text{Py}} = 1.3 \times 10^6$
 28 $\Omega^{-1}\text{m}^{-1}$ and $d_{\text{Py}} = 20 \text{ nm}$, the reference values of $P_{\text{FM}} = 0.36$ [49] and $\lambda_{\text{Py}} = 6.7 \text{ nm}$ [62], and the aforementioned

1 parameters for Pt, indicating $\Pi_s = -0.0119 \pm 0.0045$ V when the thermal conductivity of Py is $\kappa_{\text{Py}} = 22.9$ Wm⁻¹K⁻¹
 2 [72]. We note that the injection efficiency of the conduction-electron spin current, $j_s^{\text{FM}}(0)/j_s^{\text{SHE}}$, for the
 3 Pt/CoFeB(20 nm) [Pt/Py(20 nm)] interface is as low as 1.5 % (8.0 %) because of the huge difference between
 4 σ_{CoFeB} and σ_{Pt} , where the values are calculated from Eqs. (7) and (10). The injection efficiency can be intuitively
 5 understood by considering the condition of the transparent interface ($G_s = \infty$), small magnon conduction ($G_m = 0$),
 6 and $\lambda_{\text{PM}} \ll d_{\text{PM}}$; $j_s^{\text{FM}}(0)/j_s^{\text{SHE}}$ is reduced to $\Gamma_{\text{FM}}/(\Gamma_{\text{PM}} + \Gamma_{\text{FM}})$ (note that $\Gamma_{\text{PM(FM)}} \propto \sigma_{\text{PM(FM)}}$). Therefore, although
 7 the magnitude of the observed temperature modulation in the Pt/CoFeB systems is comparable to that in the Pt/Py
 8 systems, the estimated Π_s value for the Pt/CoFeB systems is much greater than that for the Pt/Py systems. Notably,
 9 the estimated Π_s values are much greater than the reported values of the SdPE coefficients, -0.0216 V for
 10 CoFeAl [49], -0.0059 V for CoFe [47], and -0.0011 V [47] and -0.0019 V [36,40,42] for Py, and even greater than
 11 the conventional (spin-independent) Peltier coefficients for CoFeB and Py [12,49], where the SdPE coefficients
 12 are estimated by multiplying the SdSE coefficients by the temperature through the Onsager reciprocal
 13 relation [8,42]. This situation remains even when taking the contribution from the interfacial thermal resistance of
 14 the PM/FM junctions into account; assuming $\kappa_{\text{int}} = 1$ GWm⁻²K⁻¹ as a typical value of the interfacial thermal
 15 conductance for metal-metal junctions [73–75], we obtained $\Pi_s = -0.062 \pm 0.022$ V and $\lambda_{\text{CoFeB}} = 18.1 \pm 9.9$ nm for
 16 the Pt/CoFeB systems, where the fitting result with κ_{int} is shown with a red dotted line in Fig. 5(b). These facts
 17 indicate that the results cannot be explained only by the conduction-electron-driven SdPE due to the SHE,
 18 indicating the substantial contribution from the magnon-driven SPE even in the metallic systems. In fact, the
 19 magnitude of the spin-current-induced temperature modulation, $\Delta A_{\text{odd}}/j_c^{\text{Pt}}$, in Pt/CoFeB (0.07×10^{-12} Km²A⁻¹ for
 20 $d_{\text{CoFeB}} = 20$ nm) and Pt/Py (0.03×10^{-12} Km²A⁻¹ for $d_{\text{Py}} = 20$ nm) films is comparable to that of the SPE in the
 21 Pt/Fe₃O₄ system (0.13×10^{-12} Km²A⁻¹ for the 23-nm-thick Fe₃O₄ layer) [44]. This is in line with a theoretical
 22 study [76], where the magnon contribution is expected to be much greater than the conduction electron
 23 contribution in PM/FM bilayers.

24 Finally, we mention remaining tasks for realizing quantitative estimation of the spin-to-heat conversion
 25 phenomena in metallic systems. As discussed above, the temperature modulation induced by the SdPE and SPE is
 26 determined by many transport parameters in PM/FM systems, and it is necessary to determine their reliable values
 27 with the aid of other experiments and calculations. Furthermore, in the PM/FM bilayer systems, thermo-spin
 28 and/or thermoelectric conversion due to the interfacial effects may have to be taken into account. For example, the
 29 spin current due to the spin anomalous Hall effect in the FM layers [77] can generate the SdPE signal and its

1 output can be modified when the spin-sink PM layer is attached. This contribution is hard to be separated from
2 other effects but is expected to be small because the modulation of the spin anomalous Hall effect cannot explain
3 the sign change of the spin-current-induced temperature modulation between the Pt/CoFeB and W/CoFeB systems.
4 Another possibility is the enhancement of the AEE due to the interfacial spin-orbit interaction, because the
5 anomalous Nernst effect, the reciprocal of the AEE, was observed to be enhanced in PM/FM multilayer films with
6 increasing the PM/FM-interface density [78]. However, such interfacial effect can be ruled out by the d_{FM}
7 dependence of the temperature modulation since the interfacial contribution is expected to decrease with
8 increasing d_{FM} , which is an opposite trend to the results shown in Fig. 5(b).

10 **IV. CONCLUSION**

11 In this paper, we reported the measurements of the temperature modulation induced by thermoelectric and
12 thermo-spin effects in PM(Pt, W, or Ta)/FM(CoFeB or Py) bilayer films and FM monolayer films by means of the
13 lock-in thermography technique. We observed clear temperature-modulation signals satisfying the symmetry of
14 the SPE, SdPE, and AEE and found that all the PM/FM bilayer films exhibit finite spin-current-induced
15 contributions, which are estimated by subtracting the AEE contribution in FM. The sign and the PM-thickness
16 dependence of the spin-current-induced temperature modulation are consistent with the interpretation that the
17 temperature modulation is driven by the SHE in PM. The CoFeB-thickness dependence of the spin-current-
18 induced temperature modulation in the Pt/CoFeB films suggests that the length scale of the observed phenomenon
19 is in the order of 10 nm. Importantly, the magnitude of the spin-current-induced temperature modulation in our
20 PM/FM bilayer films is too large to be explained only by the SdPE contribution, indicating that both the
21 conduction-electron-driven SdPE and the magnon-driven SPE contribute to the temperature modulation in our
22 films. This fact is revealed owing to the versatility of the LIT method, which allows us to overcome the difficulty
23 in conventional temperature measurements in micro-fabricated nanoscale devices. Although the quantitative
24 separation between the SPE and SdPE contributions remains to be achieved, the observation of the spin-to-heat
25 current conversion in simple metallic bilayers makes significant progresses in the physics of spin caloritronics.

27 **ACKNOWLEDGMENTS**

1 The authors thank R. Tsuboi for his assistance in the analyses of the LIT images and S. Isogami, K. Yamanoi, and
2 T. Kimura for valuable discussions. This work was supported by PRESTO “Phase Interfaces for Highly Efficient
3 Energy Utilization” (JPMJPR12C1), CREST “Creation of Innovative Core Technologies for Nano-enabled
4 Thermal Management” (JPMJCR17I1), and ERATO “Spin Quantum Rectification Project” (JPMJER1402) from
5 JST, Japan; Grant-in-Aid for Scientific Research (A) (JP15H02012), Grant-in-Aid for Scientific Research on
6 Innovative Area “Nano Spin Conversion Science” (JP26103005), and Grant-in-Aid for Specially Promoted
7 Research (JP15H05702) from JSPS KAKENHI, Japan; the Inter-University Cooperative Research Program of the
8 Institute for Materials Research, Tohoku University (17K0005); and the NEC Corporation. S.D. is supported by
9 JSPS Research Fellowships for Young Scientists (JP16J02422). Y.-C.L. is supported by JSPS International
10 Fellowship for Research in Japan (P17064).

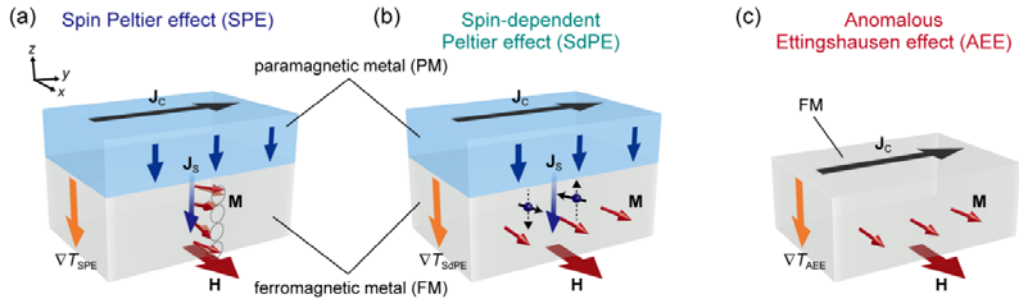
11

12 REFERENCES

- 13 [1] S. A. Wolf, D. D. Awschalom, R. A. Buhrman, J. M. Daughton, S. von Molnár, M. L. Roukes, A. Y.
14 Chtchelkanova, and D. M. Treger, *Science* **294**, 1488 (2001).
- 15 [2] I. Žutić, J. Fabian, and S. Das Sarma, *Rev. Mod. Phys.* **76**, 323 (2004).
- 16 [3] L. Gravier, S. Serrano-Guisan, F. Reuse, and J.-P. Ansermet, *Phys. Rev. B* **73**, 052410 (2006).
- 17 [4] M. Hatami, G. E. W. Bauer, Q. Zhang, and P. J. Kelly, *Phys. Rev. Lett.* **99**, 066603 (2007).
- 18 [5] H. Yu, S. Granville, D. P. Yu, and J.-P. Ansermet, *Phys. Rev. Lett.* **104**, 146601 (2010).
- 19 [6] S. Maekawa, E. Saitoh, S. O. Valenzuela, and T. Kimura, *Spin Current* (Oxford University Press, Oxford,
20 2012).
- 21 [7] T. Jungwirth, J. Wunderlich, and K. Olejník, *Nat. Mater.* **11**, 382 (2012).
- 22 [8] G. E. W. Bauer, E. Saitoh, and B. J. van Wees, *Nat. Mater.* **11**, 391 (2012).
- 23 [9] S. Maekawa, H. Adachi, K. Uchida, J. Ieda, and E. Saitoh, *J. Phys. Soc. Jpn.* **82**, 102002 (2013).
- 24 [10] B. W. Wu, G. Y. Luo, J. G. Lin, and S. Y. Huang, *Phys. Rev. B* **96**, 060402 (2017).
- 25 [11] W. Lin and C. L. Chien, arXiv:1804.01392.
- 26 [12] K. Uchida, S. Takahashi, K. Harii, J. Ieda, W. Koshibae, K. Ando, S. Maekawa, and E. Saitoh, *Nature* **455**,
27 778 (2008).
- 28 [13] K. Uchida, J. Xiao, H. Adachi, J. Ohe, S. Takahashi, J. Ieda, T. Ota, Y. Kajiwara, H. Umezawa, H. Kawai, G.
29 E. W. Bauer, S. Maekawa, and E. Saitoh, *Nat. Mater.* **9**, 894 (2010).
- 30 [14] C. M. Jaworski, J. Yang, S. Mack, D. D. Awschalom, J. P. Heremans, and R. C. Myers, *Nat. Mater.* **9**, 898
31 (2010).
- 32 [15] K. Uchida, H. Adachi, T. Ota, H. Nakayama, S. Maekawa, and E. Saitoh, *Appl. Phys. Lett.* **97**, 172505
33 (2010).
- 34 [16] C. M. Jaworski, J. Yang, S. Mack, D. D. Awschalom, R. C. Myers, and J. P. Heremans, *Phys. Rev. Lett.*
35 **106**, 186601 (2011).
- 36 [17] S. Bosu, Y. Sakuraba, K. Uchida, K. Saito, T. Ota, E. Saitoh, and K. Takanashi, *Phys. Rev. B* **83**, 224401
37 (2011).
- 38 [18] M. Weiler, M. Althammer, F. D. Czeschka, H. Huebl, M. S. Wagner, M. Opel, I.-M. Imort, G. Reiss, A.
39 Thomas, R. Gross, and S. T. B. Goennenwein, *Phys. Rev. Lett.* **108**, 106602 (2012).
- 40 [19] A. Kirihaara, K. Uchida, Y. Kajiwara, M. Ishida, Y. Nakamura, T. Manako, E. Saitoh, and S. Yoroza, *Nat.*
41 *Mater.* **11**, 686 (2012).
- 42 [20] D. Qu, S. Y. Huang, J. Hu, R. Wu, and C. L. Chien, *Phys. Rev. Lett.* **110**, 067206 (2013).

- 1 [21] T. Kikkawa, K. Uchida, Y. Shiomi, Z. Qiu, D. Hou, D. Tian, H. Nakayama, X.-F. Jin, and E. Saitoh, Phys.
2 Rev. Lett. **110**, 067207 (2013).
- 3 [22] R. Ramos, T. Kikkawa, K. Uchida, H. Adachi, I. Lucas, M. H. Aguirre, P. Algarabel, L. Morellón, S.
4 Maekawa, E. Saitoh, and M. R. Ibarra, Appl. Phys. Lett. **102**, 072413 (2013).
- 5 [23] K. Uchida, M. Ishida, T. Kikkawa, A. Kirihara, T. Murakami, and E. Saitoh, J. Phys. Condens. Matter **26**,
6 343202 (2014).
- 7 [24] R. Ramos, T. Kikkawa, M. H. Aguirre, I. Lucas, A. Anadón, T. Oyake, K. Uchida, H. Adachi, J. Shiomi, P. A.
8 Algarabel, L. Morellón, S. Maekawa, E. Saitoh, and M. R. Ibarra, Phys. Rev. B **92**, 220407 (2015).
- 9 [25] K. Uchida, H. Adachi, T. Kikkawa, A. Kirihara, M. Ishida, S. Yorozu, S. Maekawa, and E. Saitoh, Proc.
10 IEEE **104**, 1946 (2016).
- 11 [26] J. Xiao, G. E. W. Bauer, K. Uchida, E. Saitoh, and S. Maekawa, Phys. Rev. B **81**, 214418 (2010).
- 12 [27] H. Adachi, K. Uchida, E. Saitoh, and S. Maekawa, Rep. Prog. Phys. **76**, 036501 (2013).
- 13 [28] M. Schreier, A. Kamra, M. Weiler, J. Xiao, G. E. W. Bauer, R. Gross, and S. T. B. Goennenwein, Phys.
14 Rev. B **88**, 094410 (2013).
- 15 [29] U. Ritzmann, D. Hinzke, and U. Nowak, Phys. Rev. B **89**, 024409 (2014).
- 16 [30] S. M. Rezende, R. L. Rodríguez-Suárez, R. O. Cunha, A. R. Rodrigues, F. L. A. Machado, G. A. Fonseca
17 Guerra, J. C. Lopez Ortiz, and A. Azevedo, Phys. Rev. B **89**, 014416 (2014).
- 18 [31] T. Kikkawa, K. Uchida, S. Daimon, Z. Qiu, Y. Shiomi, and E. Saitoh, Phys. Rev. B **92**, 064413 (2015).
- 19 [32] V. Basso, E. Ferraro, A. Magni, A. Sola, M. Kuepferling, and M. Pasquale, Phys. Rev. B **93**, 184421
20 (2016).
- 21 [33] L. J. Cornelissen, K. J. H. Peters, G. E. W. Bauer, R. A. Duine, and B. J. van Wees, Phys. Rev. B **94**,
22 014412 (2016).
- 23 [34] Y. H. Shen, X. S. Wang, and X. R. Wang, Phys. Rev. B **94**, 014403 (2016).
- 24 [35] J. Barker and G. E. W. Bauer, Phys. Rev. Lett. **117**, 217201 (2016).
- 25 [36] A. Slachter, F. L. Bakker, J.-P. Adam, and B. J. van Wees, Nat. Phys. **6**, 879 (2010).
- 26 [37] M. Erekhinsky, F. Casanova, I. K. Schuller, and A. Sharoni, Appl. Phys. Lett. **100**, 212401 (2012).
- 27 [38] G.-M. Choi, B.-C. Min, K.-J. Lee, and D. G. Cahill, Nat. Commun. **5**, 4334 (2014).
- 28 [39] J. Flipse, F. K. Dejene, and B. J. van Wees, Phys. Rev. B **90**, 104411 (2014).
- 29 [40] J. Flipse, F. L. Bakker, A. Slachter, F. K. Dejene, and B. J. van Wees, Nat. Nanotechnol. **7**, 166 (2012).
- 30 [41] J. Flipse, F. K. Dejene, D. Wagenaar, G. E. W. Bauer, J. B. Youssef, and B. J. van Wees, Phys. Rev. Lett.
31 **113**, 027601 (2014).
- 32 [42] F. K. Dejene, J. Flipse, and B. J. van Wees, Phys. Rev. B **90**, 180402 (2014).
- 33 [43] S. Daimon, R. Iguchi, T. Hioki, E. Saitoh, and K. Uchida, Nat. Commun. **7**, 13754 (2016).
- 34 [44] K. Uchida, R. Iguchi, S. Daimon, R. Ramos, A. Anadón, I. Lucas, P. A. Algarabel, L. Morellón, M. H.
35 Aguirre, M. R. Ibarra, and E. Saitoh, Phys. Rev. B **95**, 184437 (2017).
- 36 [45] S. Daimon, K. Uchida, R. Iguchi, T. Hioki, and E. Saitoh, Phys. Rev. B **96**, 024424 (2017).
- 37 [46] R. Itoh, R. Iguchi, S. Daimon, K. Oyanagi, K. Uchida, and E. Saitoh, Phys. Rev. B **96**, 184422 (2017).
- 38 [47] T. Nomura, T. Arikawa, S. Hu, and T. Kimura, J. Phys. D: Appl. Phys. **50**, 465003 (2017).
- 39 [48] K. Yamanoi, Y. Yokotani, and T. Kimura, Phys. Rev. Appl. **8**, 054031 (2017).
- 40 [49] S. Hu, H. Itoh, and T. Kimura, NPG Asia Mater. **6**, e127 (2014).
- 41 [50] Y. K. Kato, R. C. Myers, A. C. Gossard, and D. D. Awschalom, Science **306**, 1910 (2004).
- 42 [51] J. Wunderlich, B. Kaestner, J. Sinova, and T. Jungwirth, Phys. Rev. Lett. **94**, 047204 (2005).
- 43 [52] T. Kimura, Y. Otani, T. Sato, S. Takahashi, and S. Maekawa, Phys. Rev. Lett. **98**, 156601 (2007).
- 44 [53] A. Hoffmann, IEEE Trans. Magn. **49**, 5172 (2013).
- 45 [54] J. Sinova, S. O. Valenzuela, J. Wunderlich, C. H. Back, and T. Jungwirth, Rev. Mod. Phys. **87**, 1213
46 (2015).
- 47 [55] T. Seki, R. Iguchi, K. Takanashi, and K. Uchida, Appl. Phys. Lett. **112**, 152403 (2018).
- 48 [56] H. Straube, J.-M. Wagner, and O. Breitenstein, Appl. Phys. Lett. **95**, 052107 (2009).
- 49 [57] O. Breitenstein, W. Warta, and M. Langenkamp, *Lock-in Thermography: Basics and Use for Evaluating*
50 *Electronic Devices and Materials* (Berlin, Springer Science & Business Media, 2010).
- 51 [58] H. Nakayama, K. Ando, K. Harii, T. Yoshino, R. Takahashi, Y. Kajiwara, K. Uchida, Y. Fujikawa, and E.
52 Saitoh, Phys. Rev. B **85**, 144408 (2012).
- 53 [59] C.-F. Pai, L. Liu, Y. Li, H. W. Tseng, D. C. Ralph, and R. A. Buhrman, Appl. Phys. Lett. **101**, 122404 (2012).

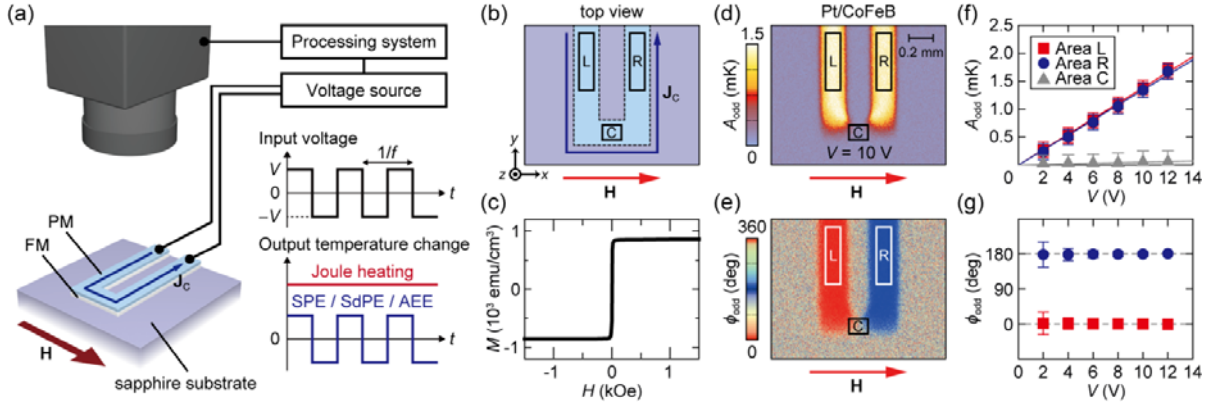
- 1 [60] Q. Hao and G. Xiao, Phys. Rev. Appl. **3**, 034009 (2015).
2 [61] J. Liu, T. Ohkubo, S. Mitani, K. Hono, and M. Hayashi, Appl. Phys. Lett. **107**, 232408 (2015).
3 [62] J. Holanda, O. Alves Santos, R. O. Cunha, J. B. S. Mendes, R. L. Rodríguez-Suárez, A. Azevedo, and S. M.
4 Rezende, Phys. Rev. B **95**, 214421 (2017).
5 [63] A. Prakash, B. Flebus, J. Brangham, F. Yang, Y. Tserkovnyak, and J. P. Heremans, Phys. Rev. B **97**,
6 020408 (2018).
7 [64] S. Fukami, T. Suzuki, Y. Nakatani, N. Ishiwata, M. Yamanouchi, S. Ikeda, N. Kasai, and H. Ohno, Appl.
8 Phys. Lett. **98**, 082504 (2011).
9 [65] S. S.-L. Zhang and S. Zhang, Phys. Rev. B **86**, 214424 (2012).
10 [66] J. Bass and W. P. Pratt, J. Phys. Condens. Matter **19**, 183201 (2007).
11 [67] C. Ahn, K.-H. Shin, and W. P. Pratt, Appl. Phys. Lett. **92**, 102509 (2008).
12 [68] C. Ahn, K.-H. Shin, R. Loloee, J. Bass, and W. P. Pratt, J. Appl. Phys. **108**, 023908 (2010).
13 [69] L. J. Cornelissen, J. Liu, R. A. Duine, J. B. Youssef, and B. J. van Wees, Nat. Phys. **11**, 1022 (2015).
14 [70] A. Anadón, R. Ramos, I. Lucas, P. A. Algarabel, L. Morellón, M. R. Ibarra, and M. H. Aguirre, Appl. Phys.
15 Lett. **109**, 012404 (2016).
16 [71] W. Zhang, W. Han, X. Jiang, S.-H. Yang, and S. S. P. Parkin, Nat. Phys. **11**, 496 (2015).
17 [72] A. D. Avery, S. J. Mason, D. Bassett, D. Wesenberg, and B. L. Zink, Phys. Rev. B **92**, 214410 (2015).
18 [73] B. C. Gundrum, D. G. Cahill, and R. S. Averback, Phys. Rev. B **72**, 245426 (2005).
19 [74] R. B. Wilson and D. G. Cahill, Phys. Rev. Lett. **108**, 255901 (2012).
20 [75] W. Wang and D. G. Cahill, Phys. Rev. Lett. **109**, 175503 (2012).
21 [76] M. Beens, J. P. Heremans, Y. Tserkovnyak, and R. A. Duine, arXiv:1804.02172.
22 [77] S. Iihama, T. Taniguchi, K. Yakushiji, A. Fukushima, Y. Shiota, S. Tsunegi, R. Hiramatsu, S. Yuasa, Y.
23 Suzuki, and H. Kubota, Nat. Electron. **1**, 120 (2018).
24 [78] K. Uchida, T. Kikkawa, T. Seki, T. Oyake, J. Shiomi, Z. Qiu, K. Takanashi, and E. Saitoh, Phys. Rev. B **92**,
25 094414 (2015).
26
27



1

2 FIG. 1 Schematic illustrations of (a) the magnon-driven spin Peltier effect (SPE) due to the spin Hall effect (SHE),
 3 (b) the conduction-electron-driven spin-dependent Peltier effect (SdPE) due to the SHE, and (c) the anomalous
 4 Ettingshausen effect (AEE). \mathbf{H} , \mathbf{M} , \mathbf{J}_c , and \mathbf{J}_s denote the magnetic field vector with the magnitude H ,
 5 magnetization vector with the magnitude M of a ferromagnetic metal (FM), charge current, and spatial direction of
 6 the spin current generated by the SHE in a paramagnetic metal (PM), respectively. ∇T_{SPE} , ∇T_{SdPE} , and ∇T_{AEE}
 7 represent the temperature gradient appearing as a result of the heat current induced by the SPE, SdPE, and AEE,
 8 respectively.

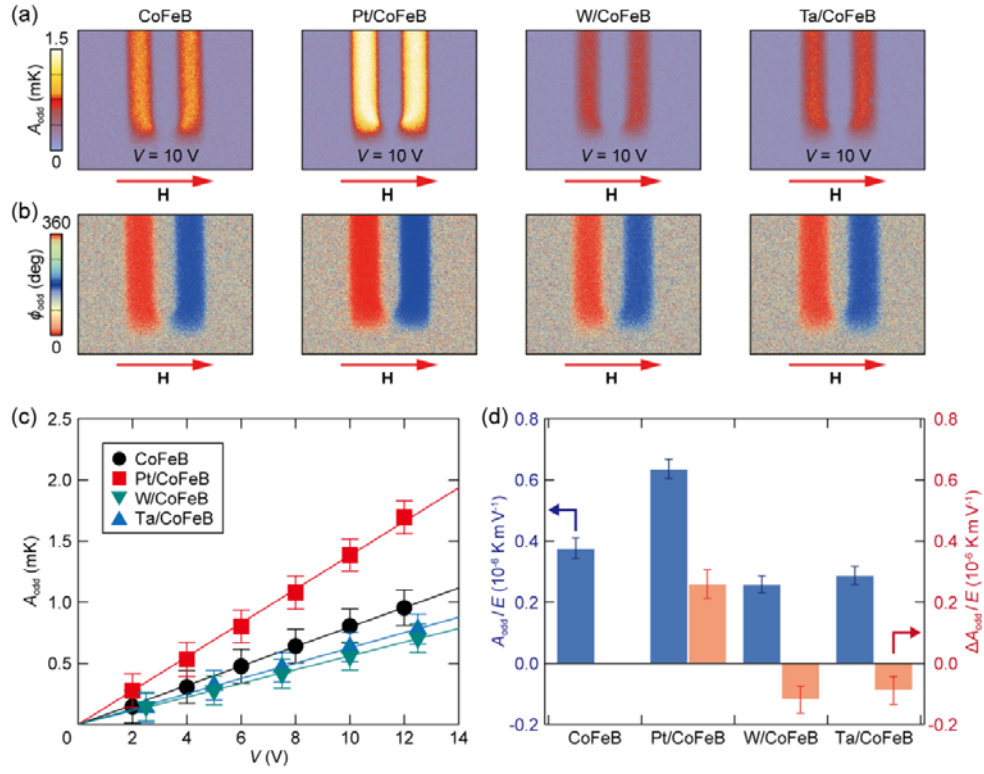
9



1

2 FIG. 2 (a) Lock-in thermography (LIT) for the measurements of the SPE, SdPE, and AEE in the PM/FM bilayer
 3 systems. V and f denote the amplitude and frequency of the rectangularly-modulated AC voltage applied to the
 4 PM/FM film. (b) Schematic of the sample system from the top view. The squares on the PM/FM film define the
 5 areas L, R, and C. (c) M - H curve for a 20-nm-thick CoFeB film on a sapphire substrate, where the H -linear
 6 contribution from the substrate was subtracted from raw data. (d),(e) A_{odd} and ϕ_{odd} images for the Pt/CoFeB film
 7 at $V = 10$ V and $|H| = 1.4$ kOe, where A_{odd} (ϕ_{odd}) denotes the lock-in amplitude (phase) of the temperature
 8 modulation with the H -odd dependence. The thickness of the Pt (CoFeB) layer is 10 nm (20 nm). (f) V
 9 dependence of A_{odd} on L, R, and C of the Pt/CoFeB film, where the plotted data were obtained by averaging the
 10 A_{odd} values on the areas. (g) V dependence of ϕ_{odd} on L and R of the Pt/CoFeB film.

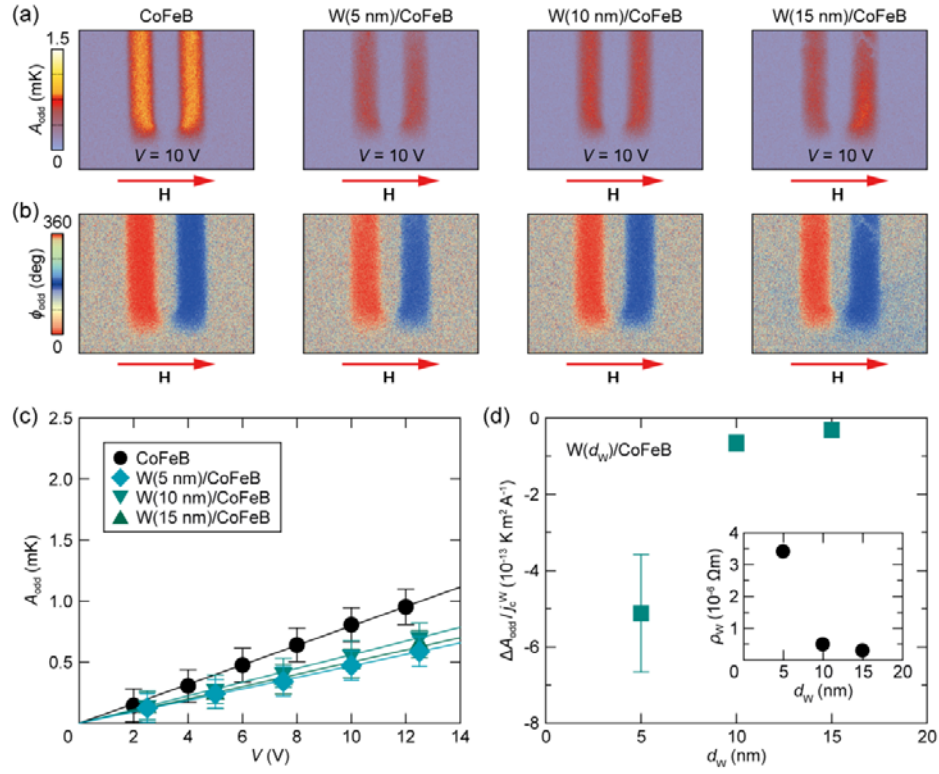
11



1

2 FIG. 3 (a),(b) A_{odd} and ϕ_{odd} images for the CoFeB monolayer and PM(Pt, W, or Ta)/CoFeB bilayer films at $V = 10$
 3 V. (c) V dependence of A_{odd} on the area L of the CoFeB and PM/CoFeB films. (d) A_{odd}/E and $\Delta A_{\text{odd}}/E$ values on L
 4 of the CoFeB and PM/CoFeB films. The ΔA_{odd} value was obtained by subtracting the A_{odd} value averaged over L
 5 of the CoFeB film from that of the PM/CoFeB film.

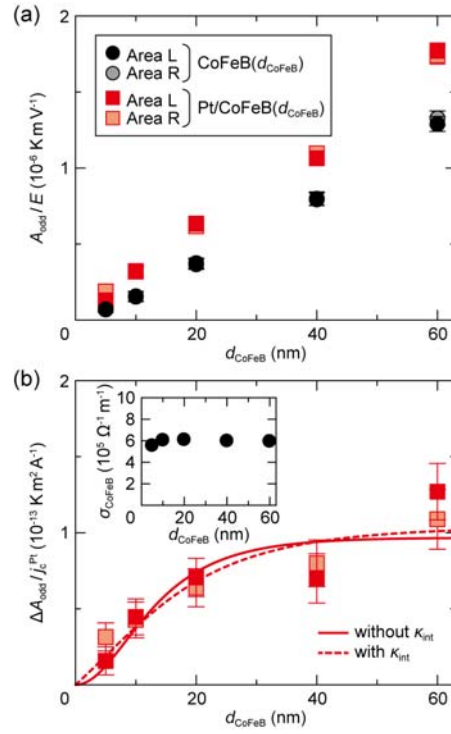
6



1

2 FIG. 4 (a),(b) A_{odd} and ϕ_{odd} images for the CoFeB monolayer and $W(d_{\text{W}})/\text{CoFeB}$ bilayer films with different W-
 3 layer thicknesses, $d_{\text{W}} = 5, 10,$ and 15 nm, at $V = 10$ V and $|H| = 0.7$ kOe. (c) V dependence of A_{odd} on the area L of
 4 the CoFeB and $W(d_{\text{W}})/\text{CoFeB}$ films. (d) d_{W} dependence of $\Delta A_{\text{odd}}/j_c^{\text{W}}$ on L of the $W(d_{\text{W}})/\text{CoFeB}$ films, where the
 5 charge-current density j_c^{W} in the W layer was estimated based on the parallel circuit model [58]. The inset to (d)
 6 shows the d_{W} dependence of the electrical resistivity ρ_{W} of the W layer.

7



1

2 FIG. 5 (a) CoFeB-thickness d_{CoFeB} dependence of A_{odd}/E on the areas L and R of the CoFeB monolayer and

3 Pt/CoFeB bilayer films. The A_{odd}/E values are estimated by linear fitting of the V dependence of A_{odd} . (b) d_{CoFeB}

4 dependence of $\Delta A_{\text{odd}}/j_c^{\text{Pt}}$ on L and R. The ΔA_{odd} value was obtained by subtracting the A_{odd} value averaged over L

5 or R of the CoFeB(d_{CoFeB}) film from that of the Pt/CoFeB(d_{CoFeB}) films. The solid (dashed) fitting curve is

6 obtained by fitting the experimental results using Eq. (12) [Eqs. (12) and (14)] for the case without (with) the

7 interfacial thermal conductance. Parameters used in the fitting are $\kappa_{\text{CoFeB}} = 29.8 \text{ W m}^{-1} \text{ K}^{-1}$ [49], $\sigma_{\text{CoFeB}} = 6.0 \times 10^5$

8 $\Omega^{-1} \text{ m}^{-1}$, $\sigma_{\text{Pt}} = 3.8 \times 10^6 \Omega^{-1} \text{ m}^{-1}$, $d_{\text{CoFeB}} = 20 \text{ nm}$, $d_{\text{Pt}} = 10 \text{ nm}$, $P_{\text{FM}}=0.72$ [64], $\lambda_{\text{Pt}} = 2 \text{ nm}$ [53], and $\theta_{\text{SH}}=0.2$ [71].

9 Here, we use $G_{\text{m}} = 0 \Omega^{-1} \text{ m}^{-2}$ to exclusively consider the SdPE contribution and an infinitely large G_{s} value to

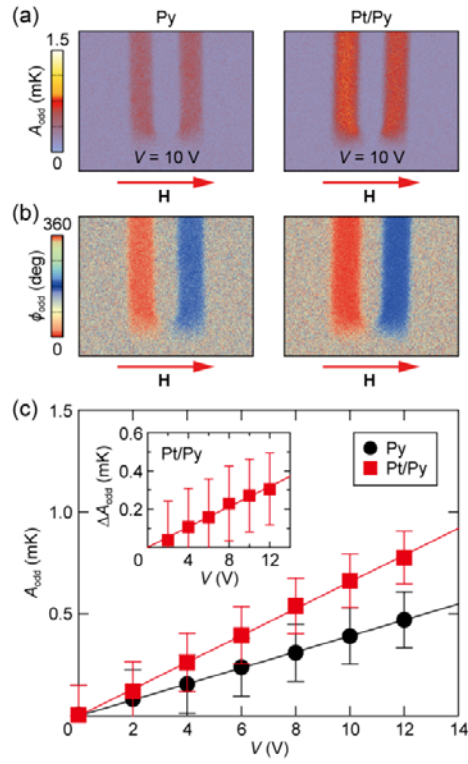
10 assume the condition that μ_{s} is continuous at the PM/FM interface. For the case without the interfacial thermal

11 conductance, $\Pi_{\text{s}} = -0.152 \pm 0.023 \text{ V}$ and $\lambda_{\text{CoFeB}} = 9.4 \pm 4.6 \text{ nm}$ are obtained. For the other case with $\kappa_{\text{int}} = 1 \text{ GW m}^{-1}$

12 K^{-1} , $\Pi_{\text{s}} = -0.062 \pm 0.022 \text{ V}$ and $\lambda_{\text{CoFeB}} = 18.1 \pm 9.9 \text{ nm}$ are obtained. The inset to (a) shows the d_{CoFeB} dependence

13 of the electrical conductivity σ_{CoFeB} of the CoFeB films.

14



1

2 FIG. 6 (a),(b) A_{odd} and ϕ_{odd} images for the Py monolayer and Pt/Py bilayer films at $V = 10$ V and $|H| = 1.4$ kOe.

3 (c) V dependence of A_{odd} on L of the Py and Pt/Py films. The inset to (c) shows the V dependence of ΔA_{odd} , where

4 the ΔA_{odd} value was obtained by subtracting the A_{odd} value averaged over L of the Py film from that of the Pt/Py

5 film.